Nanoscale

PAPER

View Article Online
View Journal | View Issue

Cite this: *Nanoscale*, 2021, **13**, 4624

MXene-encapsulated hollow Fe_3O_4 nanochains embedded in N-doped carbon nanofibers with dual electronic pathways as flexible anodes for high-performance Li-ion batteries†

Ying Guo,‡[a] Deyang Zhang,*‡[a,b] Ya Yang,[a] Yangbo Wang,[a] Zuxue Bai,[a] Paul K. Chu[b] and Yongsong Luo*[a,c]

Fe_3O_4 is one of the promising anode materials in Li-ion batteries and a potential alternative to graphite due to the high specific capacity, natural abundance, environmental benignity, non-flammability, and better safety. Nevertheless, the sluggish intrinsic reaction kinetics and huge volume variation severely limit the reversible capacity and cycling life. In order to overcome these hurdles and enhance the cycling life of Fe_3O_4, a one-dimensional (1D) nanochain structure composed of 2D Ti_3C_2-encapsulated hollow Fe_3O_4 nanospheres homogeneously embedded in N-doped carbon nanofibers (Fe_3O_4@MXene/CNFs) is designed and demonstrated as a high-performance anode in Li-ion batteries. The distinctive 1D nanochain structure not only inherits the high electrochemical activity of Fe_3O_4, but also exhibits excellent electron and ion conductivity. The Ti_3C_2 layer on the Fe_3O_4 hollow nanospheres forms the primary electron transport pathway and the N-doped carbon nanofiber network provides the secondary transport pathway. At the same time, Ti_3C_2 flakes partially accommodate the large volume change of Fe_3O_4 during Li^+ insertion/extraction. Density functional theory (DFT) calculations demonstrate that the Fe_3O_4@MXene/CNFs electrode can efficiently enhance the adsorption of Li^+ to promote Li^+ storage. As a result of the electrospinning process, self-restacking of Ti_3C_2 flakes and aggregation of Fe_3O_4 nanospheres can be prevented resulting in a larger surface area and more accessible active sites on the flexible anode. The Fe_3O_4@MXene/CNFs anode has remarkable electrochemical properties at high current densities. For example, a reversible capacity of 806 mA h g^{-1} can be achieved at 2 A g^{-1} even after 500 cycles, corresponding to an area specific capacity of 1.612 mA h cm^{-2} at 4 mA cm^{-2} and a capacity as high as 613 mA h g^{-1} is retained at 5 A g^{-1}, corresponding to an area capacity of 1.226 mA h cm^{-2} at 10 mA cm^{-2}. The results indicate that the Fe_3O_4@MXene/CNFs anode has excellent properties for Li-ion storage.

Received 31st December 2020,
Accepted 12th February 2021

DOI: 10.1039/d0nr09228b

rsc.li/nanoscale

Introduction

Challenges and opportunities coexist in the development of lithium-ion batteries (LIBs)[1] as efforts are made to address the increasing demand for batteries with high energy and high power.[2] Conventional commercial graphite anodes have a capacity of only 372 mA h g^{-1} in Li-ion batteries and therefore, new anodes with higher energy density, power capability, cost effectiveness, stability, and cycling lifetime without risk of explosion are highly desirable for medium and large-scale energy-storage applications.[3,4]

Transition metal oxides (TMOs) such as NiO, CuO_2, Co_3O_4, MnO_2, and Fe_3O_4 have higher capacities than commercial graphite anodes[5] and magnetic oxide (Fe_3O_4) has also been demonstrated to be a promising candidate because of the high theoretical capacity in LIBs (~1000 mA h g^{-1}),[6] nontoxicity, high natural abundance (iron being the fourth most abundant element in the earth crust), and low cost.[7–9] In addition, recent studies have found that in the Fe_3O_4/Li cell, the reduced metallic Fe^0 can continue to store spin-polarized electrons during the discharging process at low voltage showing an anoma-

[a]*Key Laboratory of Microelectronics and Energy of Henan Province, Henan Joint International Research Laboratory of New Energy Storage Technology, Engineering Research Center for MXene Energy Storage Materials of Henan Province, Xinyang Normal University, Xinyang 464000, P. R. China. E-mail: ysluo@xynu.edu.cn, zdy@xynu.edu.cn; Tel: +86 376 6391760; Fax: +86 376 6391760*
[b]*Department of Physics, Department of Materials Science & Engineering, and Department of Biomedical Engineering, City University of Hong Kong, Tat Chee Avenue, KowloonHong Kong, China*
[c]*College of Physics and Electronic Engineering, Nanyang Normal University, Nanyang 473061, China*

†Electronic supplementary information (ESI) available. See DOI: 10.1039/d0nr09228b

‡These authors contributed equally to this work.

lously high storage capacity beyond its theoretical value.[10] However, the key challenge for Fe_3O_4 anodes in LIBs is the low capacity retention during cycling caused by the low intrinsic electrical conductivity, severe particle aggregation and coarsening of small Fe nanoparticles,[11,12] and large volume expansion/contraction (as high as 100%), consequently resulting in large deformation, internal stress, and poor reliability.[13] It has been also shown that accumulation of the internal passivation phase leads to capacity attenuation and reduced rate performance during cycling.[14] More seriously, the large volume change during lithiation/delithiation causes electrode pulverization and the active materials may even peel off from the current collector giving rise to large irreversible capacity loss and poor cycling stability.[15,16]

Much effort has been made to synthesize nanostructured electrode materials with different morphologies such as nanoflowers,[6] nanodots,[13] pomegranate-like,[17] and cornlike[18] to improve the properties of Fe_3O_4-based anode materials. Although reducing the particle size to the nanometer range can address the internal strain during charging–discharging and decreases the distances for ion and electron transport,[19] the cycling performance is still limited due to undesirable electrode/electrolyte reactions, aggregation of Fe_3O_4 nanoparticles (NPs), and repeated decomposition/formation of solid electrolyte interphase (SEI) films stemming from cyclic exposure of the surface to the electrolyte.[20] Nanostructured carbon materials such as graphitic carbon,[21] CNT,[22] and graphene,[23,24] incorporated with metal oxides can improve the electrochemical performance.[25] For example, metal oxide nanoparticles anchored on graphene show improved reversible capacity and cyclic characteristics because 2D graphene sheets serve as a highly conductive matrix and immobilize the nanoparticles, thereby effectively buffering the volume change during the charging/discharging process.[24] Furthermore, confinement of metal oxide NPs between graphene layers prevents cracking during cycling.

On the heels of recent development of graphene/metal oxide anode materials, other 2D materials such as a family of transition metal carbides and nitrides (named MXenes) have aroused considerable attention because of their unique physical and chemical properties.[26,27] MXenes have the general formula of $M_{n+1}X_nT_x$, where T represents the surface functional group such as –OH, –O, and –F. For example, $Ti_3C_2T_x$ is prepared by selective etching of Al of the Ti_3AlC_2 MAX phase.[26] MXenes are attractive in energy storage and conversion applications by virtue of the high electrical conductivity, abundant surface functional groups, and excellent dispersion in various solvents.[28] Nevertheless, similar to other 2D materials, MXene nanosheets are inclined to stacking *via* van der Waals interactions consequently resulting in limited active sites, sluggish kinetics, and compromised electrochemical properties.[29] It has been proved that 2D MXene flakes can be made into 1D nanofibers which not only prevent agglomeration and protect the flakes, but also improve the electrical conductivity of the nanofibers.[30] Recently, in the research of Gogotsi *et al.*, electrospun MXene/carbon nanofibers have been considered as an effective method to prevent the self-restacking of MXene in the effort to produce more flexible, stable, and durable composites.[31]

The insulating and electrochemically inactive binders commonly found in conventional LIB electrodes cause uneven active materials distribution and poor contact between the materials and substrates[32] and therefore, binder-free nanostructured electrodes prepared by electrospinning have advantages including the large surface area,[33] robust adhesion to the substrate, high areal/specific capacity, fast electron/ion transfer,[34] and free space to alleviate volume expansion.[35] Here, in the pursuit of better cycling stability and rate capability, a free-standing 3D reticular composite composed of 2D Ti_3C_2-encapsulated hollow Fe_3O_4 nanospheres uniformly embedded in N-doped carbon nanofibers is designed and prepared by electrospinning and annealing in this work. The 0D@2D/1D nanochain structure (denoted as Fe_3O_4@MXene/CNFs) constitutes a flexible electrode for high-performance LIBs. As shown in Fig. 1, the MXene ultra-thin nanosheets are obtained by etching and exfoliating the MAX phase. The PDDA-modified hollow Fe_3O_4 nanospheres and ultrathin MXene nanosheets are self-assembled electrostatically in the DMF solution and PAN is added to obtain the black spinning solution. The Fe_3O_4/MXene/PAN nanofibers are prepared by electrospinning at a high voltage and carbonized under a protective gas to form Fe_3O_4@MXene/CNFs. In this structure, the MXene and carbon nanofibers provide dual electronic pathways.[36] The Ti_3C_2 layer on the Fe_3O_4 hollow nanospheres is the primary electron transport pathway and the N-doped carbon nanofibers form the secondary electron pathway. Moreover, the nanochains create the cushion to accommodate the volume expansion of Fe_3O_4 and contribute to the formation of a more stable SEI (solid electrolyte interphase) film to improve the cyclic stability. In addition, the Fe_3O_4@MXene/CNFs electrode can efficiently enhance the adsorption of Li^+, which has been demonstrated by DFT calculations. As a result, the Fe_3O_4@MXene/CNFs composite shows a high specific capacity (1786 mA h g^{-1}), excellent capacity retention (reversible capacity of 806 mA h g^{-1} at a current density of 2 A g^{-1} after 500 cycles), and remarkable area specific capacities(1.612 mA h cm^{-2} at 4 mA cm^{-2}).

Results and discussion

The structure and morphology are characterized by scanning electron microscopy (SEM) and atomic force microscopy (AFM). The Ti_3AlC_2 powders (~≤10 μm) have some slightly layered texture, but it appears to be seamless (Fig. S1a–c†). Simultaneously, Fig. S1d† shows the XRD pattern of the Ti_3AlC_2 powders. SEM image of Ti_3C_2 (Fig. S5a_{1-4}†) shows that ultra-thin Ti_3C_2 flakes are successfully prepared by etching and stripping Ti_3AlC_2 the powders. As indicated from the atomic force microscopy (AFM) measurements (Fig. 2d_{1-2}), vast majority of the MXene nanosheets have a uniform thickness of 2–3 nm with a lateral size of 1–3μm. In consideration of that

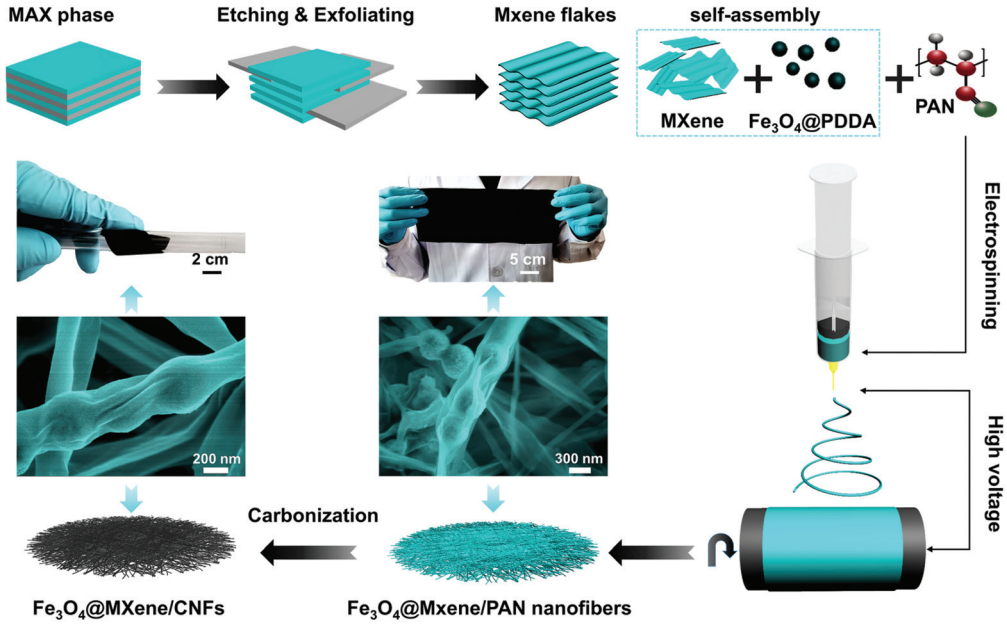

Fig. 1 Schematic illustration of the multi-step fabrication procedures of Fe_3O_4@MXene/CNFs nanocomposites.

the theoretical thickness of a single Ti_3C_2 layer is ~1.5 nm, the 2 nm-thick nanosheet should be nearly monolayer Ti_3C_2.[37] The Fe_3O_4 nanoparticles are disclosed to have uniform spherical morphology with an average particle size of 470.76 nm (Fig. S2a$_{1-3}$ and Fig. S3†) and it is confirmed to be magnetic iron oxide Fe_3O_4 (PDF# 89-2712) (Fig. S8b†).

Following the "nanochains" strategy of the electrospinning process, Ti_3C_2 MXene-encapsulated hollow Fe_3O_4 nanospheres are threaded into PAN fibers. In order to unravel the electrostatic self-assembled mechanism acting on above structural establishment, zeta (ζ) potential measurements are carried out on different samples as shown in Fig. S4.† The Fe_3O_4 nanospheres modified by PDDA are positively charged and the Mxene nanosheets are negatively charged. Due to electrostatic attraction, these two oppositely charged nano materials are attracted to each other and self-assembled into the Fe_3O_4@MXene superlattice.[38] The Fe_3O_4 nanospheres have a transparent gauze coating (ultra-thin Ti_3C_2) (Fig. 2a$_{1-3}$). No obvious aggregation is observed and the as-threaded components are uniformly covered by PAN, which can guarantee the further development of the 3D hierarchical network. After stabilization and carbonization, the hierarchical structure remains intact with a tightened surface (Fig. 2b$_{1-3}$). The carbonized fibers are interconnected without structure collapse or aggregation. As shown in Fig. 2c$_{1-3}$, the as-prepared flexible Fe_3O_4@MXene/CNFs film can be directly tailored into free-standing working electrodes which can be folded repeatedly hundreds of times without damage. On the contrary, On the contrary, Fe_3O_4/CNFs (Fig. S2c$_{1-3}$†) obtained by carbonization of Fe_3O_4/PAN nanofibers (Fig. S2b$_{1-3}$†) exhibit severe crimping. The Fe_3O_4/CNFs electrodes have less flexibility than Fe_3O_4@MXene/CNFs electrodes (Fig. S6†) due to the excellent bending rigidities of the Ti_3C_2 MXene, which makes the electrode more stable.[39] As shown in Fig. S7,† Fe_3O_4@MXene/CNFs film also shows excellent tensile resistance. A simple stress–strain test shows that a thin film with a mass of 0.0012 g and an area of 6 cm^2 can lift a weight more than 2083 times its mass. This indicates that Fe_3O_4@MXene/CNFs electrode has great mechanical properties. Different from the above composites, both the MXene/PAN nanofibers (Fig. S5b$_{1-4}$†) and MXene/CNFs (Fig. S5c$_{1-4}$†) have a nanoribbon structure due to the high MXene loading.[31]

The interior nanostructure and chemical composition of Fe_3O_4@MXene/CNFs are further investigated by transmission electron microscopy (TEM) and EDS mapping. Fig. 3a shows that the MXene-encapsulated Fe_3O_4 nanospheres are threaded into the carbon nanofibers with a nanochain structure and the Fe_3O_4 nanospheres have a hollow structure, which is consistent with the results of the SEM images. As shown in Fig. 3b and c, the nearly monolayer MXene is coupled and coated on the Fe_3O_4 nanospheres to form efficient electron pathway and also buffer/inhibit the volume change of Fe_3O_4 nanospheres during charging and discharging. Fig. 3d shows the magnification of the yellow box in Fig. 3c which clearly shows the structure of Fe_3O_4@mxene/CNFs and a carbon shell thickness of about 2 nm. The High-resolution TEM (HRTEM) image (Fig. 3e) indicates the hexagonal structure of the basal planes and high crystallinity of the MXene flakes in the fibers without obvious nanometer-scale defects.[37,40] The crystal structure with obvious lattice fringes of 0.26 nm corresponds to the *d*-spacing of the (100) plane of Ti_3C_2, again demonstrating the existence of Ti_3C_2 in the composite.[41] The Fast Fourier Transform patterns image (Fig. 3f) indicates the hexagonal symmetry (*P*63/*mmc* space group) of Ti_3C_2 nanosheets with a

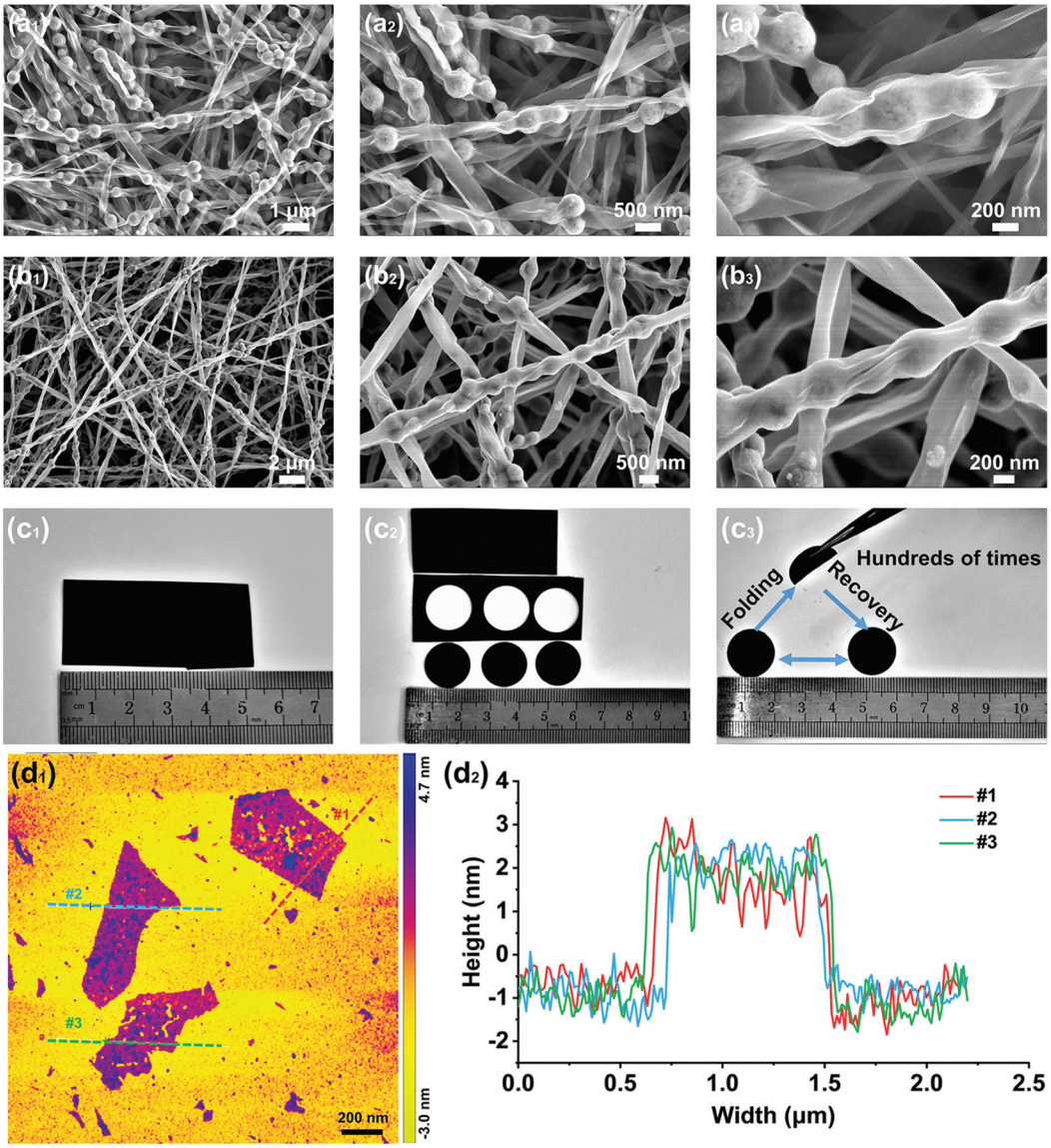

Fig. 2 SEM images of Fe_3O_4/MXene/PAN fibers (a_{1-3}), and Fe_3O_4@MXene/CNFs (b_{1-3}); Digital photographs of the flexible Fe_3O_4@MXene/CNFs film and flexible test (c_{1-3}); AFM image (d_1) and thickness distribution (d_2) of the Ti_3C_2 nanosheet.

parameter ($a = b = 3.073$ Å, and $c = 18.557$ Å) in line with previous reports.[37,42] Fig. 3g and h show well-defined lattice fringes with *d*-spacings of 0.25, 0.48, and 0.30 nm corresponding to the (311), (111) and (220) planes of magnetic iron oxide Fe_3O_4. The corresponding element mapping images (Fig. 3i) also disclose reasonable distributions of C, N, Ti, Fe, and O in the fiber.

XRD, XPS, and Raman scattering are conducted to further study the structure and composition. Fig. 4a shows the XRD patterns of the MXene flakes, Fe_3O_4 nanospheres, and Fe_3O_4@MXene/CNFs. The diffraction peaks can be indexed to magnetic iron oxide (PDF#89-2712). The Ti_3C_2 (002) peak at 6.46° from the composite weakens indicating that electrospinning mitigates restacking of the Ti_3C_2 nanosheets.[43] Fig. S8a and c† display the XRD patterns of MXene/CNFs and Fe_3O_4/CNFs respectively. As shown in Fig. 4b, the two major peaks in the Fe 2p XPS spectrum of Fe_3O_4@MXene/CNFs at 710.9 and 724.9 eV correspond to Fe $2p_{3/2}$ and Fe $2p_{1/2}$. The Fe $2p_{3/2}$ spectrum can be deconvolved into two peaks at 710.7 and 713.3 eV, whereas the Fe $2p_{1/2}$ peak comprises two peaks at 723.6 and 725.7 eV. The peaks at 713.3 and 725.7 eV can be assigned to Fe(III) in Fe_3O_4.[21] In the high-resolution Ti 2p spectrum in Fig. 4c, the Fe_3O_4@MXene/CNFs exhibit tow remarkably Ti–O–Fe covalent bonds located at 458.9 eV and 464.4 eV, verifying the strong interaction between them.[44–46] The peaks at 457.8 and 463.6 eV are associated with the $2p_{3/2}$ and $2p_{1/2}$ orbits of Ti^{3+} in Ti_3C_2 MXene.[47,48] As for the high resolution C 1s XPS spectrum (Fig. 4d) reveals the presence of C–Ti (283.6 eV), C–C (284.6 eV), C═N (286.1 eV) and O–C═O (288.5 eV) in Fe_3O_4@MXene/CNFs,[41] whereas the high-resolution N 1s spec-

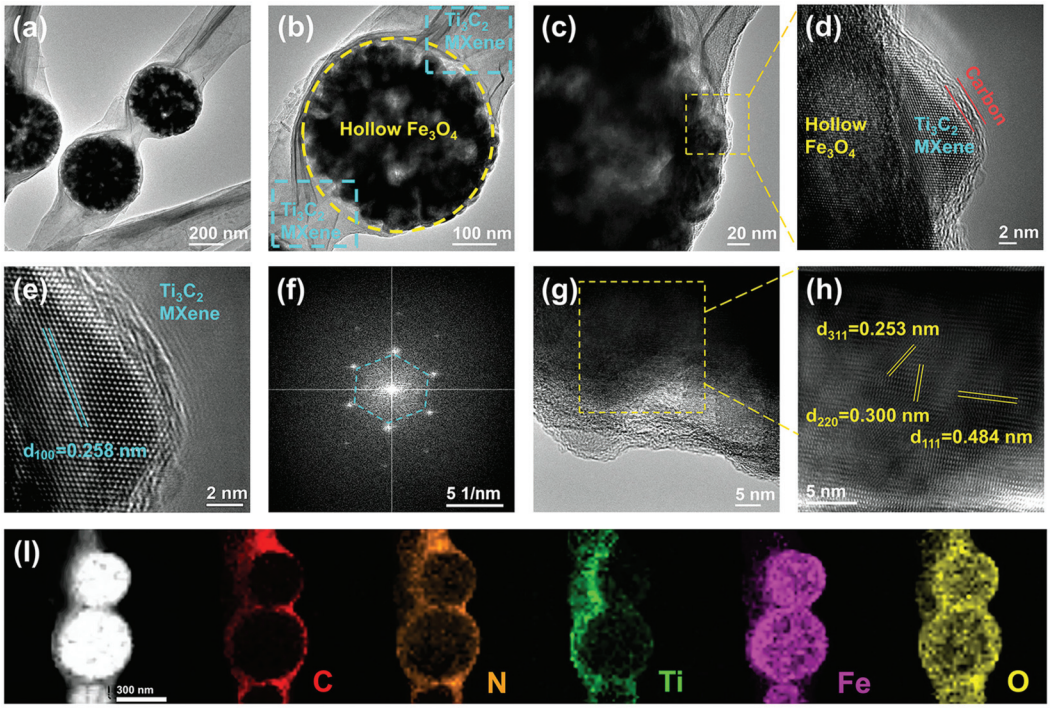

Fig. 3 (a–c) TEM images of Fe_3O_4@MXene/CNFs; (d, e, g and h) HRTEM images of Fe_3O_4@MXene/CNFs; (f) The Fast Fourier Transform (FFT) pattern and image of (e); (i) Elemental mapping images of Fe_3O_4@MXene/CNFs.

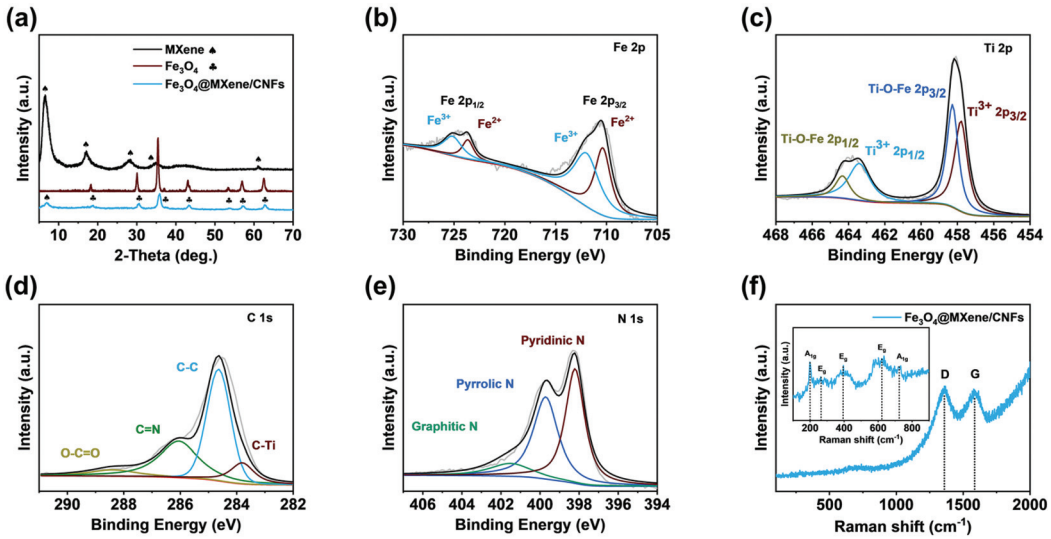

Fig. 4 (a) XRD patterns of MXene flakes, Fe_3O_4 and Fe_3O_4@MXene/CNFs; High-resolution XPS spectra of (b) Fe 2p (c) Ti 2p (d) C 1s and (e) N 1s of Fe_3O_4@MXene/CNFs; (f) Raman spectra of the Fe_3O_4@MXene/CNFs (Top-left inset shows the partial enlargement).

trum of Fe_3O_4@MXene/CNFs (Fig. 4e) shows three peaks at 398.7 eV, 399.5 eV, and 401.2 eV corresponding to pyridinic-N, pyrrolic-N, and graphitic-N, respectively.[49,50] These results confirm that nitrogen atoms from PAN are introduced to CNFs during pyrolysis. The N atoms in CNFs increase the electron concentration and lower the Fermi lever of CNFs to improve the electrical conductivity.[51]

The Raman scattering spectrum of Fe_3O_4@MXene/CNFs (Fig. 4f) shows the representative bands including the A_{1g} out-of-plane vibration modes at 195 cm^{-1} for Ti and 712 cm^{-1} for C atoms. The E_g group vibrations for the in-plane modes of Ti, C, and surface functional group are observed at 281, 361, and 630 cm^{-1}, respectively.[52,53] There is no evidence of TiO_2 (150 cm^{-1}) and the two broad peaks at 1348 and 1587 cm^{-1} are

related to the defect-induced mode and E_{2g2} graphitic mode of amorphous carbon, respectively, with an intensity ratio ($R = I_D/I_G$) of 1.03, which is consistent with the TEM results.[8] The results indicate the presence of low-crystallinity carbon with an amorphous structure which facilitates diffusion of Li^+ and offers more intercalation sites for Li ion storage.[54] The carbon content in the Fe_3O_4@MXene/CNFs composite is calculated to be about 26% based on the thermogravimetric analysis (TGA; Fig. S9†) and the reasonable carbon loading enhances the initial coulombic efficiency in lithium-ion batteries.[55]

The Fe_3O_4@MXene/CNFs, MXene/CNFs, and Fe_3O_4/CNFs freestanding electrodes are made into anodes for lithium-ion batteries to evaluate the electrochemical properties and energy storage mechanism. Fig. 5a shows the initial three successive CV curves of the Fe_3O_4@MXene/CNFs in the voltage range of 0.01–3 V *vs.* Li/Li^+ at a scan rate of 0.2 mV s^{-1}. During the first cathode scan, a weaker reduction peak at about 1.0 V could be found, which can be attributed to the formation of $Li_xFe_3O_4$. Besides, there is a significant reduction peak at 0.51 V which disappeared in the next scans. It corresponds to the insertion of lithium ions and the formation of SEI films meanwhile Fe^{3+}

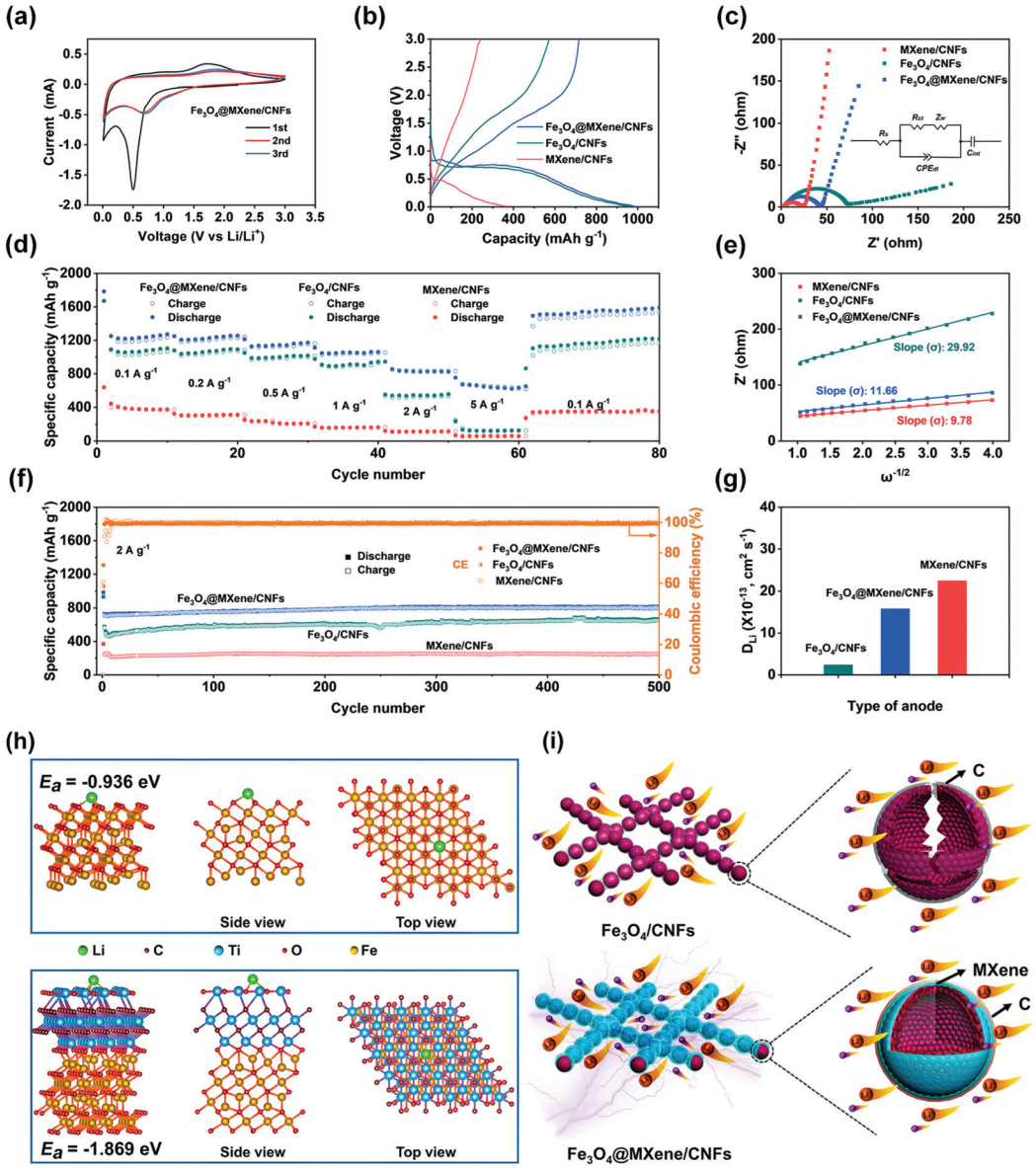

Fig. 5 (a) Cyclic voltammograms for the initial three cycles of the Fe_3O_4@MXene/CNFs electrode at a scanning rate of 0.2 mV s^{-1}; (b) comparison of the first galvanostatic charge/discharge curves of Fe_3O_4@MXene/CNFs, Fe_3O_4/CNFs, and MXene/CNFs at 2 A g^{-1}; (c) Nyquist plots of Fe_3O_4@MXene/CNFs, Fe_3O_4/CNFs, and MXene/CNFs electrodes; (d) rate performance of Fe_3O_4@MXene/CNFs, Fe_3O_4/CNFs, and MXene/CNFs at different current densities; (e) Warburg coefficients of Fe_3O_4@MXene/CNFs, Fe_3O_4/CNFs, and MXene/CNFs electrodes; (f) cycling performance of Fe_3O_4@MXene/CNFs, Fe_3O_4/CNFs, and MXene/CNFs at a large current density of 2 A g^{-1}; (g) Li^+ transport coefficients of Fe_3O_4@MXene/CNFs, Fe_3O_4/CNFs, and MXene/CNFs electrodes; (h) DFT simulation of the lithium adsorption configuration; (i) diagram of ion/electron transport.

or Fe^{2+} is reduced to Fe^0. The anodic peak at 1.75 V represents gradual oxidation of Fe^0 to $Li_xFe_3O_4$ and Fe^{3+}. Starting from the second cycle, the reduction peak moves to 0.6 V caused by reduced polarization of iron oxide.[56,57] Additionally, the CV curves of Fe_3O_4@MXene/CNFs in subsequent cycles almost overlap implying the high reversibility. The Li^+ intercalation process can be described as follows:

$$Fe_3O_4 + xLi^+ + xe^- \leftrightarrow Li_xFe_3O_4 \quad (1)$$

$$Li_xFe_3O_4 + (8-x)Li^+ + (8-x)e^- \leftrightarrow 3Fe + 4LiO_2 \quad (2)$$

$$Fe_3O_4 + 8Li^+ + 8e^- \leftrightarrow 3Fe + 4LiO_2 \quad (3)$$

The electrochemical reaction of Fe_3O_4 with Li^+ includes multiple steps.[58] During the discharging process, Fe_3O_4 reacts with Li^+ to form $Li_xFe_3O_4$ and then $Li_xFe_3O_4$ is reduced into Fe and Li_2O. During the charging process, Fe reacts with Li_2O while it is oxidized gradually to Fe_3O_4. The specific reactions are shown in eqn (1) and (2) and the overall reaction is shown in eqn (3).

Fig. 5b shows the comparison of the first galvanostatic charging/discharging curves of Fe_3O_4@MXene/CNFs, MXene/CNFs, and Fe_3O_4/CNFs at 2 A g^{-1}. The initial discharge capacity (mA h g^{-1}) and initial coulombic efficiency (CE) of Fe_3O_4@MXene/CNFs, MXene/CNFs, and Fe_3O_4/CNFs are 985.92/72.01%, 373.03/62.59%, and 921.44/59.88%, respectively (Table S1†). It is obvious that the Fe_3O_4@MXene/CNFs electrode has the highest initial coulombic efficiency. The low CE value is attributed to the irreversible reactions including interfacial reactions and formation of the solid electrolyte interphase (SEI) film. Therefore, the amount of Li^+ trapped in the defects/holes and consumed by the SEI film of Fe_3O_4@MXene/CNFs electrodes is less than that of MXene/CNFs and Fe_3O_4/CNFs. The larger the carbon content, the lower is the initial coulombic efficiency, which corresponds to the TGA results mentioned above. The galvanostatic discharging/charging curves of MXene/CNFs, Fe_3O_4/CNFs, and Fe_3O_4@MXene/CNFs at different cycles (1st, 2nd, 3rd, 100th, 200th, and 300th cycles) acquired at a current density of 2 A g^{-1} are shown in Fig. S10a–c.† There are no evident discharge/charge voltage plateaus in the discharging/charging curves of MXene/CNFs showing the typical capacitive characteristics. The charging–discharging curves of Fe_3O_4@MXene/CNFs for both the 200th and 300th cycles almost overlap indicating that lithiation and delithiation are stable after several hundred cycles. In comparison, the charging and discharging curves of Fe_3O_4/CNFs for different cycles are relatively scattered, indicating that the SEI film is continuously broken/recombined. After 100 cycles, the Fe_3O_4/CNFs and Fe_3O_4@MXene/CNFs electrodes are examined by SEM. Fig. S11a$_{1-3}$† shows that after 100 cycles, the Fe_3O_4@MXene/CNFs electrode retains the original morphology but the surface of the Fe_3O_4/CNFs electrode shows cracks (Fig. S11b$_{1-3}$†). The surface cracks on Fe_3O_4/CNFs may be caused by the large volume change of Fe_3O_4 nanospheres during charging and discharging. Fe_3O_4@MXene/CNFs maintains the good morphology due to the excellent bending rigidity of Ti_3C_2 MXene and ability to accommodate the volume change while providing channels for fast transmission of Li ions during charging and discharging (Fig. 5i).

Fig. 5c shows the Nyquist plots of the MXene/CNFs, Fe_3O_4/CNFs, and Fe_3O_4@MXene/CNFs electrodes. The Nyquist plots show a semicircle in the medium high frequency region ascribed to the charge-transfer resistance (R_{ct}) and a sloping line in the low frequency region which corresponds to the Warburg impedance associated with diffusion of lithium ions.[59] The impedance parameters obtained by fitting with the equivalent circuit are listed in Table S2.† The R_{ct} values of MXene/CNFs, Fe_3O_4/CNFs and Fe_3O_4@MXene/CNFs electrodes are 17.59, 73.43, and 36.88 Ω, respectively, demonstrating that Ti_3C_2 reduces the charge transfer impedance of Fe_3O_4/CNFs. The larger slope of the Warburg line suggests better ion conductivity of the electrode materials.[60] In this respect, MXene/CNFs possesses the highest ion conductivity and Ti_3C_2 enhances the conductivity of Fe_3O_4/CNFs. In order to assess Li^+ diffusion at the electrode/electrolyte interface, the diffusion coefficients of lithium ions (D_{Li}) are determined by Eqn (4)–(6):[61]

$$\omega = 2\pi f \quad (4)$$

$$Z' = R_s + R_{ct} + \sigma\omega^{-0.5} \quad (5)$$

$$D_{Li} = 0.5R^2T^2/A^2n^4F^4C^2\sigma^2 \quad (6)$$

where R is the gas constant (8.314 J mol^{-1} K^{-1}), σ is the Warburg coefficient, T is the Kelvin temperature (293.15 K), A is the contact area of the electrode (2.01 cm^2), n is the electron number per molecule during the oxidization, F is Faraday constant (96 485 C mol^{-1}) and C is the molar concentration of Li^+. The values of σ are derived from the linear relation between Z' (the real parts of impedance) and ω (angular frequency), corresponding values of D_{Li} are subsequently calculated from eqn (6). The Warburg coefficients of MXene/CNFs, Fe_3O_4/CNFs and Fe_3O_4@MXene/CNFs are 9.78, 29.92, and 11.66, respectively (Fig. 5e) and the diffusion coefficients of lithium ions (D_{Li}) of MXene/CNFs, Fe_3O_4/CNFs, and Fe_3O_4@MXene/CNFs are 2.24 × 10^{-12}, 2.39 × 10^{-13}, and 1.58 × 10^{-12} cm^2 s^{-1}, respectively (Fig. 5g). The results indicate the significant positive effects of Ti_3C_2 MXene on improving electron and ion transport.

Fe_3O_4@MXene/CNFs not only shows a faster ion/electron transfer rate and more stable structure, but also has a better adsorption capacity for Li ions. To elucidate the mechanism, DFT calculation is conducted to investigate the Li adsorption ability of the different electrode materials (Fig. 5h). The adsorption energies (E_a) of MXene/CNFs, Fe_3O_4/CNFs, and Fe_3O_4@MXene/CNFs for lithium ions are −2.159, −0.936, and −1.869 eV, respectively (Table S3†) indicating that Fe_3O_4@MXene/CNFs has better Li-adsorption ability than Fe_3O_4/CNFs. It is because the coating of MXene changes the configuration at the interface and improves the electrochemical performance of Fe_3O_4@MXene/CNFs. Therefore, we can conclude that the coating of MXene is beneficial to

enhance the Li adsorption and optimized the interface engineering.

To further evaluate the electrochemical properties of the electrodes, the rate performance is shown in Fig. 5d. Fe_3O_4@MXene/CNFs has the highest specific capacity and optimal rate performance. Discharge capacities of 1259.3, 1245.1, 1160.9, 1049.5, 827.0, and 629.5 mA h g^{-1} are exhibited at current densities of 0.1, 0.2, 0.5, 1, 2, and 5 A g^{-1}, respectively. When the current density is returned to 0.1 A g^{-1}, the capacity is 1586.5 mA h g^{-1}, which is even higher than that in the initial cycles because of electrode activation.[62] It is worth noting that the capacity of Fe_3O_4/CNFs decreases significantly at a large current density of 5 A g^{-1} because lithium ions do not have enough time to diffuse at the high current density. Based on the electrochemical properties mentioned above, Fe_3O_4@MXene/CNFs exhibits the highest discharge specific capacity, optimum rate performance and cycle stability. The enhanced Li^+ storage capability for the composite electrode can be attribute to the coherent synergistic effect of Fe_3O_4 and MXene as well as the doping of N atoms. Fig. 5f presents the cycling performance of the samples at a current density of 2 A g^{-1}. The discharge capacity of Fe_3O_4@MXene/CNFs is 800.9 mA h g^{-1} after 500 cycles, which is actually larger than that observed after the 5th cycle (716.8 mA h g^{-1}) indicative of lithium-induced reactivation of the electrode. This phenomenon is widely observed in previously reported works about TMOs and their composites.[63,64] In comparison, Fe_3O_4/CNFs shows a capacity of only 612 mA h g^{-1} after 500 cycles due to destruction of Fe_3O_4 nanospheres during cycling. Our results show that the 3D conductive network and dual conductive pathways enhance the cycling stability of Fe_3O_4. We also compare electrochemical performance of various Fe_xO_y-based anode materials for LIBs in Table S4,† from which it is evident that our Fe_3O_4@MXene/CNFs clearly stands out and outperforms other composite systems, especially under high current density. The excellent electrochemical performance of Fe_3O_4@MXene/CNFs anodes can be attributed to the following facts: (i) the composite material not only inherits the high electrochemical activity of Fe_3O_4, but also the unique Mxene coating provides the primary fast electron transport path for electrochemical reaction and alleviates the volume expansion of Fe_3O_4; (ii) DFT calculation shows that Mxene coating can effectively enhance the lithium ion adsorption ability of composite electrode materials; (iii) the N-doped carbon nanofibers derived from PAN provide a second fast electron transport path for the electrode reaction.

In most cases, the loading of active materials (mg cm^{-2}) and area specific capacity (mA h cm^{-2}) are two important parameters to evaluate the free-standing and flexible electrodes. For Fe_3O_4@MXene/CNFs electrode, the mass of a single electrode is about 0.0040 g, the area is 2 cm^2, and the mass per unit area is 2 mg cm^2. Fig. S12a† shows the area specific capacities at different rates (0.2–10 mA cm^{-2}), and Fig. S12b† shows a remarkable area specific capacity of 1.612 mA h cm^{-2} at 4 mA cm^{-2} after 500 cycles. Considering the practicality of energy storage devices, the excellent performances led us to design a full-cell with the commercial $LiCoO_2$ cathode and the Fe_3O_4@MXene/CNFs anode (Fig. S12c†). As shown in Fig. S12d,† the full-cell exhibits a superior electrochemical performance with a higher reversible specific capacity of 530 mA h g^{-1} at 0.5 A g^{-1}. These results indicate that the Fe_3O_4@MXene/CNFs anode has a powerful potential for practical applications.

Conclusions

In summary, the free-standing and flexible Fe_3O_4@MXene/CNFs composite is prepared by electrospinning. Design of the dual electronic pathways composed of Ti_3C_2 MXene and N-doped carbon nanofibers not only greatly enhance the electrical and ionic conductivity but also keeps the structure of Fe_3O_4 nanospheres stable during cycling. In addition, self-restacking of Ti_3C_2 and aggregation of Fe_3O_4 are reduced significantly and as a result, there are more accessible active sites on the flexible anode. The Fe_3O_4@MXene/CNFs composite shows a high specific capacity (1786 mA h g^{-1}), excellent capacity retention (reversible capacity of 806 mA h g^{-1} at a current density of 2 A g^{-1} after 500 cycles), and remarkable area capacities(1.612 mA h cm^{-2} at 4 mA cm^{-2}). The results reveal a viable strategy to design and prepare low-cost and stable electrode materials for LIBs and the technique can be readily extended to the fabrication of other types of functional nanomaterials in energy storage, electromagnetic shielding, and catalysis.

Conflicts of interest

There are no conflicts to declare.

Acknowledgements

This work was financially supported by the National Natural Science Foundation of China (No. 61574122 and 61874093), Zhongyuan Thousand Talents Plan-Science & Technology Innovation Leading Talents Project (No. 194200510009), Key Scientific Research Projects of Higher Education Institutions in Henan Province (19A430023), Nanhu Scholars Program for Young Scholars of XYNU, and City University of Hong Kong Strategic Research Grants (No. 7005105 and 7005264). This work was also supported by the Xinyang Normal University Analysis & Testing Center.

References

1 Y. Liu, Y. Zhu and Y. Cui, *Nat. Energy*, 2019, **4**, 540–550.
2 F. Wu, J. Maier and Y. Yu, *Chem. Soc. Rev.*, 2020, **49**, 1569–1614.
3 M. Armand and J. M. Tarascon, *Nature*, 2008, **451**, 652–657.

4 Y. Gao, F. Zheng, D. Wang and B. Wang, *Nanoscale*, 2020, **12**, 20100–20117.
5 P. Poizot, S. Laruelle, S. Grugeon, L. Dupont and J. M. Tarascon, *Nature*, 2000, **407**, 496–499.
6 F. X. Ma, H. Hu, H. B. Wu, C. Y. Xu, Z. Xu, L. Zhen and X. W. Lou, *Adv. Mater.*, 2015, **27**, 4097–4101.
7 F. Wu and G. Yushin, *Energy Environ. Sci.*, 2017, **10**, 435–459.
8 G. Xia, Q. Gao, D. Sun and X. Yu, *Small*, 2017, **13**, 1701561.
9 Q. Li, J. Zhou, F. Li and Z. Sun, *Inorg. Chem. Front.*, 2020, **7**, 3491–3499.
10 Q. Li, H. Li, Q. Xia, Z. Hu, Y. Zhu, S. Yan, C. Ge, Q. Zhang, X. Wang, X. Shang, S. Fan, Y. Long, L. Gu, G. X. Miao, G. Yu and J. S. Moodera, *Nat. Mater.*, 2021, **20**, 76–83.
11 X. Xu, J. Liu, Z. Liu, J. Shen, R. Hu, J. Liu, L. Ouyang, L. Zhang and M. Zhu, *ACS Nano*, 2017, **11**, 9033–9040.
12 X. Xu, J. Feng, J. Liu, F. Lv, R. Hu, F. Fang, L. Yang, L. Ouyang and M. Zhu, *Electrochim. Acta*, 2019, **312**, 224–233.
13 G. Zhong, K. Qu, C. Ren, Y. Su, B. Fu, M. Zi, L. Dai, Q. Xiao, J. Xu, X. Zhong, F. An, M. Ye, S. Ke, S. Xie, J. Wang, P. Gao and J. Li, *Nano Energy*, 2020, **74**, 104876.
14 J. Li, S. Hwang, F. Guo, S. Li, Z. Chen, R. Kou, K. Sun, C. J. Sun, H. Gan, A. Yu, E. A. Stach, H. Zhou and D. Su, *Nat. Commun.*, 2019, **10**, 2224.
15 D. Kong, J. Luo, Y. Wang, W. Ren, T. Yu, Y. Luo, Y. Yang and C. Cheng, *Adv. Funct. Mater.*, 2014, **24**, 3815–3826.
16 V. Etacheri, R. Marom, R. Elazari, G. Salitra and D. Aurbach, *Energy Environ. Sci.*, 2011, **4**, 3243.
17 D. Han, G. Guo, Y. Yan, T. Li, B. Wang and A. Dong, *Energy Stor. Mater.*, 2018, **10**, 32–39.
18 Y. Wang, L. Chen, H. Liu, Z. Xiong, L. Zhao, S. Liu, C. Huang and Y. Zhao, *Chem. Eng. J.*, 2019, **356**, 746–755.
19 K. Zhao, L. Zhang, R. Xia, Y. Dong, W. Xu, C. Niu, L. He, M. Yan, L. Qu and L. Mai, *Small*, 2016, **12**, 588–594.
20 X. Zhao, X. Li, S. Zhang, J. Long, Y. Huang, R. Wang and J. Sha, *J. Mater. Chem. A*, 2017, **5**, 23592–23599.
21 Z. Shi, Q. Zhang, L. Zhao, H. Wang and W. Zhou, *ACS Appl. Mater. Interfaces*, 2020, **12**, 15043–15052.
22 X. Wang, X. Liu, G. Wang, Y. Xia and H. Wang, *J. Mater. Chem. A*, 2016, **4**, 18532–18542.
23 Y. Zuo, G. Wang, J. Peng, G. Li, Y. Ma, F. Yu, B. Dai, X. Guo and C.-P. Wong, *J. Mater. Chem. A*, 2016, **4**, 2453–2460.
24 M. Huang, C. Chen, S. Wu and X. Tian, *J. Mater. Chem. A*, 2017, **5**, 23035–23042.
25 M. Srivastava, J. Singh, T. Kuila, R. K. Layek, N. H. Kim and J. H. Lee, *Nanoscale*, 2015, **7**, 4820–4868.
26 B. Anasori, M. R. Lukatskaya and Y. Gogotsi, *Nat. Rev. Mater.*, 2017, **2**, 16098.
27 A. Zhang, R. Liu, J. Tian, W. Huang and J. Liu, *Chem. – Eur. J.*, 2020, **26**, 6342–6359.
28 K. T. Sarang, X. Zhao, D. Holta, M. Radovic, M. J. Green, E.-S. Oh and J. L. Lutkenhaus, *Nanoscale*, 2020, **12**, 20699–20709.
29 K. Li, M. Liang, H. Wang, X. Wang, Y. Huang, J. Coelho, S. Pinilla, Y. Zhang, F. Qi, V. Nicolosi and Y. Xu, *Adv. Funct. Mater.*, 2020, **30**, 2000842.
30 A. Levitt, J. Zhang, G. Dion, Y. Gogotsi and J. M. Razal, *Adv. Funct. Mater.*, 2020, **30**, 2000739.
31 A. S. Levitt, M. Alhabeb, C. B. Hatter, A. Sarycheva, G. Dion and Y. Gogotsi, *J. Mater. Chem. A*, 2019, **7**, 269–277.
32 L. Zhang, X. Qin, S. Zhao, A. Wang, J. Luo, Z. L. Wang, F. Kang, Z. Lin and B. Li, *Adv. Mater.*, 2020, **32**, 1908445.
33 X. Li, W. Chen, Q. Qian, H. Huang, Y. Chen, Z. Wang, Q. Chen, J. Yang, J. Li and Y. W. Mai, *Adv. Energy Mater.*, 2020, **11**, 2000845.
34 L. Han, M. Zhang, H. Wang, P. Li, W. Wei, J. Shi, M. Huang, Z. Shi, W. Liu and S. Chen, *Nanoscale*, 2020, **12**, 24477–24487.
35 A. Singh and V. Kalra, *J. Mater. Chem. A*, 2019, **7**, 11613–11650.
36 J. S. Lee, M. S. Jo, R. Saroha, D. S. Jung, Y. H. Seon, J. S. Lee, Y. C. Kang, D. W. Kang and J. S. Cho, *Small*, 2020, **16**, 2002213.
37 L. Ding, Y. Wei, L. Li, T. Zhang, H. Wang, J. Xue, L. X. Ding, S. Wang, J. Caro and Y. Gogotsi, *Nat. Commun.*, 2018, **9**, 155.
38 P. Xiong, X. Zhang, F. Zhang, D. Yi, J. Zhang, B. Sun, H. Tian, D. Shanmukaraj, T. Rojo, M. Armand, R. Ma, T. Sasaki and G. Wang, *ACS Nano*, 2018, **12**, 12337–12346.
39 M. Kurtoglu, M. Naguib, Y. Gogotsi and M. W. Barsoum, *MRS Commun.*, 2012, **2**, 133–137.
40 C. Peng, X. Yang, Y. Li, H. Yu, H. Wang and F. Peng, *ACS Appl. Mater. Interfaces*, 2016, **8**, 6051–6060.
41 W. Eom, H. Shin, R. B. Ambade, S. H. Lee, K. H. Lee, D. J. Kang and T. H. Han, *Nat. Commun.*, 2020, **11**, 2825.
42 H. Chen, Y. Wen, Y. Qi, Q. Zhao, L. Qu and C. Li, *Adv. Funct. Mater.*, 2019, **30**, 1906996.
43 D. Xu, K. Ma, L. Chen, Y. Hu, H. Jiang and C. Li, *Chem. Eng. Sci.*, 2020, **212**, 115342.
44 Y. Wang, Y. Li, Z. Qiu, X. Wu, P. Zhou, T. Zhou, J. Zhao, Z. Miao, J. Zhou and S. Zhuo, *J. Mater. Chem. A*, 2018, **6**, 11189–11197.
45 J. Yan, C. E. Ren, K. Maleski, C. B. Hatter, B. Anasori, P. Urbankowski, A. Sarycheva and Y. Gogotsi, *Adv. Funct. Mater.*, 2017, **27**, 1701264.
46 L. Hong, S. Ju, Y. Yang, J. Zheng, G. Xia, Z. Huang, X. Liu and X. Yu, *Sustainable Energy Fuels*, 2020, **4**, 2352–2362.
47 X. Wu, Z. Wang, M. Yu, L. Xiu and J. Qiu, *Adv. Mater.*, 2017, **29**, 1607017.
48 L. Yu, Z. Fan, Y. Shao, Z. Tian, J. Sun and Z. Liu, *Adv. Energy Mater.*, 2019, **9**, 1901839.
49 Q. Pang, J. Tang, H. Huang, X. Liang, C. Hart, K. C. Tam and L. F. Nazar, *Adv. Mater.*, 2015, **27**, 6021–6028.
50 T. Wang, S. Shi, Y. Li, M. Zhao, X. Chang, D. Wu, H. Wang, L. Peng, P. Wang and G. Yang, *ACS Appl. Mater. Interfaces*, 2016, **8**, 33091–33101.
51 Q. Liu, J. Hou, Q. Hao, P. Huang, C. Xu, Q. Zhou, J. Zhou and H. Liu, *Nanoscale*, 2020, **12**, 22778–22786.
52 P. Zhang, R. A. Soomro, Z. Guan, N. Sun and B. Xu, *Energy Stor. Mater.*, 2020, **29**, 163–171.
53 R. Lotfi, M. Naguib, D. E. Yilmaz, J. Nanda and A. C. T. van Duin, *J. Mater. Chem. A*, 2018, **6**, 12733–12743.

54 B. Guo, W. Du, T. Yang, J. Deng, D. Liu, Y. Qi, J. Jiang, S. J. Bao and M. Xu, *Adv. Sci.*, 2020, **7**, 1902617.
55 H. Huang, J. Wang, X. Yang, R. Hu, J. Liu, L. Zhang and M. Zhu, *Angew. Chem., Int. Ed. Engl.*, 2020, **59**, 14504–14510.
56 X. Jiang, X. Yang, Y. Zhu, Y. Yao, P. Zhao and C. Li, *J. Mater. Chem. A*, 2015, **3**, 2361–2369.
57 F. X. Ma, H. B. Wu, C. Y. Xu, L. Zhen and X. W. Lou, *Nanoscale*, 2015, **7**, 4411–4414.
58 Y. Yang, W. Yuan, X. Zhang, C. Wang, Y. Yuan, Y. Huang, Y. Ye, Z. Qiu and Y. Tang, *Renewable Sustainable Energy Rev.*, 2020, **127**, 109884.
59 T. Zhang, L. Zhang, L. Zhao, X. Huang, W. Li, T. Li, T. Shen, S. Sun and Y. Hou, *Small*, 2020, **16**, 2005302.
60 D. Wang, Y. Yu, H. He, J. Wang, W. Zhou and H. D. Abruna, *ACS Nano*, 2015, **9**, 1775–1781.
61 X. Yang and A. L. Rogach, *Adv. Energy Mater.*, 2019, **9**, 1900747.
62 W. Gou, X. Kong, Y. Wang, Y. Ai, S. Liang, A. Pan and G. Cao, *Chem. Eng. J.*, 2019, **374**, 545–553.
63 H. Sun, G. Xin, T. Hu, M. Yu, D. Shao, X. Sun and J. Lian, *Nat. Commun.*, 2014, **5**, 4526.
64 X. Hu, M. Ma, M. Zeng, Y. Sun, L. Chen, Y. Xue, T. Zhang, X. Ai, R. G. Mendes, M. H. Rummeli and L. Fu, *ACS Appl. Mater. Interfaces*, 2014, **6**, 22527–22533.